nature nanotechnology

Article

https://doi.org/10.1038/s41565-023-01513-0

# A wearable aptamer nanobiosensor for non-invasive female hormone monitoring

Received: 15 March 2023

Accepted: 24 August 2023

Published online: 28 September 2023

Check for updates

Cui Ye[1,2], Minqiang Wang[1,2], Jihong Min[1], Roland Yingjie Tay[1], Heather Lukas[1], Juliane R. Sempionatto[1], Jiahong Li[1], Changhao Xu[1] & Wei Gao[1]

Personalized monitoring of female hormones (for example, oestradiol) is of great interest in fertility and women's health. However, existing approaches usually require invasive blood draws and/or bulky analytical laboratory equipment, making them hard to implement at home. Here we report a skin-interfaced wearable aptamer nanobiosensor based on target-induced strand displacement for automatic and non-invasive monitoring of oestradiol via in situ sweat analysis. The reagentless, amplification-free and 'signal-on' detection approach coupled with a gold nanoparticle-MXene-based detection electrode offers extraordinary sensitivity with an ultra-low limit of detection of 0.14 pM. This fully integrated system is capable of autonomous sweat induction at rest via iontophoresis, precise microfluidic sweat sampling controlled via capillary bursting valves, real-time oestradiol analysis and calibration with simultaneously collected multivariate information (that is, temperature, pH and ionic strength), as well as signal processing and wireless communication with a user interface (for example, smartphone). We validated the technology in human participants. Our data indicate a cyclical fluctuation in sweat oestradiol during menstrual cycles, and a high correlation between sweat and blood oestradiol was identified. Our study opens up the potential for wearable sensors for non-invasive, personalized reproductive hormone monitoring.

Female hormones affect much of women's health, from menstruation to pregnancy to menopause and more (for example, depression)[1,2]. They are regulated by the feedback mechanism of the hypothalamic–pituitary–ovarian axis, which governs all the female hormonal events related to reproductive activity. Oestradiol is the primary form of the female hormone oestrogen, and the most potent and prevalent female hormone during the reproductive years. During the menstrual cycle, oestradiol provides feedback to the hypothalamic–pituitary–ovarian axis to regulate the production of luteinizing hormone and ovulation (Fig. 1a)[3]. In addition to its centrality in sexual development, it markedly affects major organs, including the blood vessels, bones, muscles and brain, in both males and females[4–7]. Therefore, oestradiol monitoring is important in human biology from the cradle to the grave, and is an essential component of infertility management as well as general physiological surveillance[8,9]. Compared to other alternative approaches for fertility monitoring based on the basal thermometer or urine luteinizing hormone, serum oestradiol provides the most timely and accurate information[10]. Moreover, serum oestradiol analysis is a gold standard for monitoring the induction of ovulation with gonadotrophins[11]; routine oestradiol monitoring plays a crucial role for women in menopause and individuals undergoing hormone replacement therapy[12,13]. Despite the widespread importance of female hormones, our ability to measure

[1]Andrew and Peggy Cherng Department of Medical Engineering, Division of Engineering and Applied Science, California Institute of Technology, Pasadena, CA, USA. [2]These authors contributed equally: Cui Ye, Minqiang Wang. e-mail: weigao@caltech.edu

https://doi.org/10.1038/s41565-023-01513-0

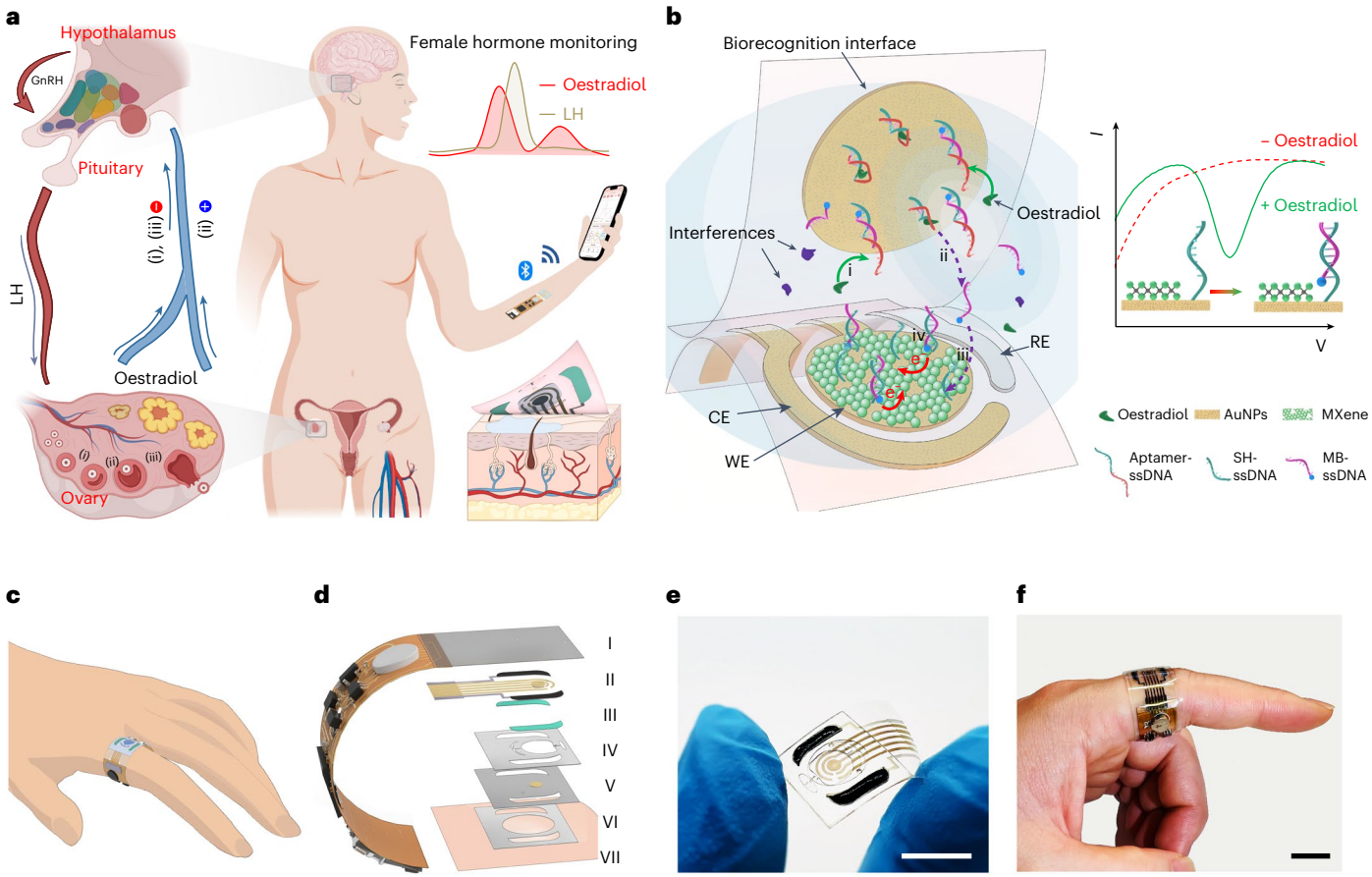


**Fig. 1 | A wearable nanobiosensor based on strand-displacement aptamer switch for non-invasive reagentless female reproductive hormone analysis.** **a**, Female hormones play an important role in women's health; non-invasive monitoring of oestradiol can be realized through sweat analysis using a skin-interfaced wearable sensor: (i) follicular phase; (ii) ovulation; (iii) luteal phase. GnRH, gonadotropin-releasing hormone; LH, luteinizing hormone; +, stimulatory effect; −, inhibitory effect. **b**, The reagentless in situ quantification of oestradiol using a AuNPs–MXene sensor coupled with a target-induced strand-displacement aptamer switch. i to iv represent recognition of the oestradiol molecule by the aptamer on the biorecognition interface (i), targetrecognition-induced strand displacement to release the MB-ssDNA (ii), recapture of thereleased MB-ssDNA by the SH-ssDNA on the working electrode (WE) (iii), and electrochemicalquantification of the methylene blue from the recaptured MB-ssDNA on the working electrode (iv). CE, counter electrode; RE, reference electrode. **c**,**d**, Schematic (**c**) and layered design (**d**) of the flexible and wireless microfluidic wearable patch for automatic sweat induction via iontophoresis, precise sampling via CBVs and reagentless aptamer-based oestradiol analysis. Sections I to VII represent plastic substrate interfacing with the FPCB (I), inkjet-printed sensor array (II), carbachol-loaded hydrogels (carbagels) (III), microfluidic channels (IV), biorecognition interface (V), sweat accumulation layer (VI) and the skin (VII). **e**,**f**, Photographs of a disposable sensor patch (**e**) and a fully integrated wireless wearable patch worn on a finger (**f**) for female hormone monitoring. Scale bars, 1 cm.

them properly has not kept pace with their growing importance in clinical medicine[8,14].

Quantitative measurements of female hormones have been obtained by mass spectrometry and immunoassays that require bulky equipment and have low detection throughput for routine clinical use[15]. Quantifying pM-level oestradiol in the menstruation cycle appears to be a crucial and challenging issue for infertility identification (Fig. 1a)[16–18]. Moreover, these approaches are typically based on invasive blood draws and complex sample preparation, making them impractical for at-home remote use[19]. Although there are commercially available 'at-home' oestrogen test kits based on finger-prick blood drop, saliva or 24-hour urine, they all require the collected samples to be sent out for lengthy laboratory analysis. Highly sensitive and accurate on-site quantification of oestradiol levels in non-invasively accessible biological fluids is highly desired to ensure optimal medical decision-making at the individual level[20].

Human sweat contains rich molecular information on an individual's health state[21–25]. The transition from traditional laboratory analysis to wearable sweat analysis could enable non-invasive and remote female hormone monitoring[26–30]. In situ monitoring of sweat female hormones is challenging due to the extremely low concentration (picomolar level) and variations in sweat accessibility and sample matrix[30], and thus has yet to be realized.

In this work, we introduce a wireless wearable sensor based on a target-induced strand-displacement aptamer switch for in situ automatic electrochemical monitoring of female hormones with subpicomolar sensitivity (Fig. 1b and Supplementary Fig. 1). The flexible sensor contains a biorecognition interface modified with an oestradiol-selective deoxyribonucleic acid (DNA) aptamer facing a gold nanoparticles–MXene (AuNPs–MXene)-based detection working electrode modified with capture single-stranded DNA (ssDNA) for indirect target detection. These parallel faces function as walls of the microfluidic reservoir and are bridged on sweat filling. When the sensor is exposed to body fluids such as sweat, oestradiol molecules competitively bind with the oestradiol aptamer, resulting in the release of the redox probe methylene blue-tagged ssDNA (MB-ssDNA) molecules from the biorecognition interface, which are then captured by the opposite detection working electrode through

complementary DNA hybridization. Sensitive and selective oestradiol quantification is realized through the detection of the methylene blue redox signal on the AuNPs–MXene working electrode (Fig. 1b and Supplementary Fig. 2). The use of AuNPs–MXene improves the electron transport efficiency for the methylene blue reduction, enabling the assay analysis with ultra-high sensitivity. This nanoengineered sensor patch is mass-producible at low cost through inkjet printing with custom-developed nanomaterial inks (Supplementary Fig. 3 and Supplementary Tables 1 and 2). $Ti_3C_2T_x$ MXene, a two-dimensional (2D) transition metal carbide, was chosen because it showed the highest conductivity among solution-processed 2D materials and had surface hydrophilicity for ink formulation and antifouling[31,32].

A fully integrated wearable system was developed to realize automatic sweat oestradiol sensing. This system contains a microfluidic iontophoresis module for autonomous sweat induction and sampling at rest (without the need for vigorous exercise), a potentiometric pH sensor, a resistive skin temperature sensor and an impedimetric ionic strength sensor for real-time sensor calibration (to mitigate the influence of inter- and/or intrapersonal variations), as well as electronic circuitry for signal processing and wireless communication (Fig. 1c,d and Supplementary Fig. 4). The miniaturized wearable system was designed to be mechanically flexible and conform to the human skin (Fig. 1e,f and Supplementary Fig. 5). We validated the sensor against gold-standard measurements and in human participants for personalized female hormone analysis during menstrual cycles.

## Results and discussion

### Design and characterization of the oestradiol nanobiosensor

The reagentless oestradiol sensor design was based on a strand-displacement aptamer switch. At the biorecognition interface, the oestradiol aptamer-ssDNA is immobilized on a AuNPs-decorated surface, forming a partially hybridized duplex with an MB-ssDNA probe molecule, which acts as a competitive redox probe (Fig. 2a and Supplementary Fig. 6). Considering that a short MB-ssDNA with weak but selective affinity reaction to the oestradiol aptamer is desired for efficient target-induced strand-displacement reaction, a 25-base MB-ssDNA was selected on the basis of secondary structure analysis of the oestradiol aptamer[33,34]: a substantial hybridization reaction was obtained from the 25-base MB-ssDNA but not from the molecules with 24 or fewer bases (Supplementary Fig. 7). On the detection working electrode, a capture thiolated ssDNA (SH-ssDNA) molecule, the antisense strand of the MB-ssDNA probe molecule, is immobilized on a AuNPs–MXene electrode (Supplementary Fig. 8). In the presence of oestradiol, the MB-ssDNA is released by the aptamer-ssDNA because of the higher affinity of the aptamer to oestradiol than the partially hybridized sequence[35], and then anneals to the complementary sequence at the working electrode (Fig. 2a). The recaptured MB-ssDNA probe molecules can be quantified by the redox signal measured electrochemically via a square wave voltammogram (SWV). The reagentless 'signal-on' detection approach, coupled with highly sensitive low-background SWV measurements, offers extraordinary sensitivity and applicability for ultra-low-level sweat oestradiol analysis in situ[36].

The biorecognition interface and the detection working electrode were prepared by scalable inkjet printing of AuNPs (roughly 22 nm), which offered a high electrochemical active surface area (ECSA) for subsequent nucleic acid modifications (Fig. 2b and Supplementary Figs. 9 and 10). On the working electrode, a thin layer of MXene, was inkjet-printed on the surface of AuNPs to further improve the sensor performance (Fig. 2b,c and Supplementary Fig. 11). The MXene nanosheets used in the ink were largely single- or few-layered (Supplementary Fig. 12), and the sheet size was smaller than 0.45 μm (Supplementary Fig. 13). Scanning electron microscopy (SEM) characterizations and experimentally obtained double layer capacitance (linearly correlated with ECSA) confirmed higher ECSA of the AuNPs–MXene electrode than those of evaporated Au and printed AuNPs electrodes (Supplementary Fig. 10). Compared to traditional screen printing, inkjet printing has multiple advantages here including lower cost due to less ink consumption, lower risk for sample contamination, more precise spatial and thickness control of the printed nanomaterials and higher electroactive surface area due to the porous structures to realize optimal oestradiol sensing (Supplementary Figs. 14 and 15)[37]. Differential pulse voltammograms (DPV) and open circuit potential–electrochemical impedance spectroscopy (OCP–EIS) were used to further characterize the AuNPs–MXene electrode surface after each modification step (Fig. 2d,e). The increased peak current height in DPV voltammograms and the decreased resistance in Nyquist plots after MXene printing indicate the increased electrode conductivity and electrochemical catalytic activities. The following increased resistance in Nyquist plots and decreased DPV peak current height and after SH-ssDNA and 6-mercapto-1-hexanol (MCH) modification indicate that the self-assembled monolayers and the SH-ssDNA molecules impede the charge transfer at the electrode–solution interface due to the increased surface coverage by non-conductive molecules. It should be noted that despite MXene's high conductivity, the bare inkjet-printed MXene electrode (without AuNPs support) showed large impedance due to the lack of percolating pathway in the ultrathin film of MXene flakes. After incubation with 50 pM of oestradiol, a clear methylene blue redox peak appeared at roughly −0.28 V, demonstrating the successful capture of MB-ssDNA released from the biorecognition interface due to oestradiol–aptamer interaction (Fig. 2f). The incubation time, reagent concentration and measurement frequency were further optimized to reach the optimal sensor performance with high sensitivity and repeatability (Supplementary Figs. 16 and 17 and Supplementary Note 1).

Our study shows that both AuNPs and MXene play a crucial role in sensor performance (Fig. 2g and Supplementary Fig. 18). Compared to the plain Au electrode, the AuNPs coating increased the effective electrode area, thus increasing the SH-ssDNA loading capacity for improved sensitivity. A further 40% signal enhancement was obtained with the additional MXene layer. This can be explained by MXene's ultra-high electrical conductivity[38], which facilitates the electrode conductivity and the efficiency of charge transfer and transport for the reduction of methylene blue molecules. The importance of MXene was further validated by introducing 2-mercaptopropionic acid (MPA) to block the surface of MXene via the esterification interactions between the −COOH groups in the MPA and the −OH groups in the MXene. The resultant AuNPs–MXene-MPA electrode showed a substantially decreased signal, indicating the crucial role of the MXene layer for highly sensitive oestradiol analysis (Fig. 2g). It should be noted that the possible methylene blue reduction caused by MXene does not affect the final SWV oestradiol quantification as the initial phase of the negative SWV scan will transform methylene blue to the oxidized state; highly stable SWV measurements were observed on MB-ssDNA- and SH-ssDNA-modified AuNPs–MXene electrodes over 5,000 repetitive scans and after 0–120 minutes of solution conditioning (Supplementary Figs. 19 and 20). The oestradiol sensors also displayed high operation stability in solution and high dry-state long-term storage stability under cold and room temperature conditions (Supplementary Figs. 21 and 22). The sensors from five different batches displayed high repeatability with a low coefficient of variation of 0.013 (Supplementary Fig. 22a).

The sensor performance was evaluated by SWV in artificial sweat (0.2× PBS, pH 7.4) containing physiologically relevant oestradiol levels (0.1–100 pM) (Fig. 2h). The sensor exhibited a log-linear relationship between peak current density height of the SWV voltammograms and target concentrations with an ultra-low limit of detection of 0.14 pM (Fig. 2i). The oestradiol sensor demonstrated high selectivity to oestradiol over a variety of potential interferences present at much higher concentrations (Fig. 2j). The accuracy of the aptamer sensors for sweat oestradiol analysis was validated by the enzyme-linked immunosorbent assay (ELISA) using iontophoresis-induced sweat samples (Fig. 2k),

https://doi.org/10.1038/s41565-023-01513-0

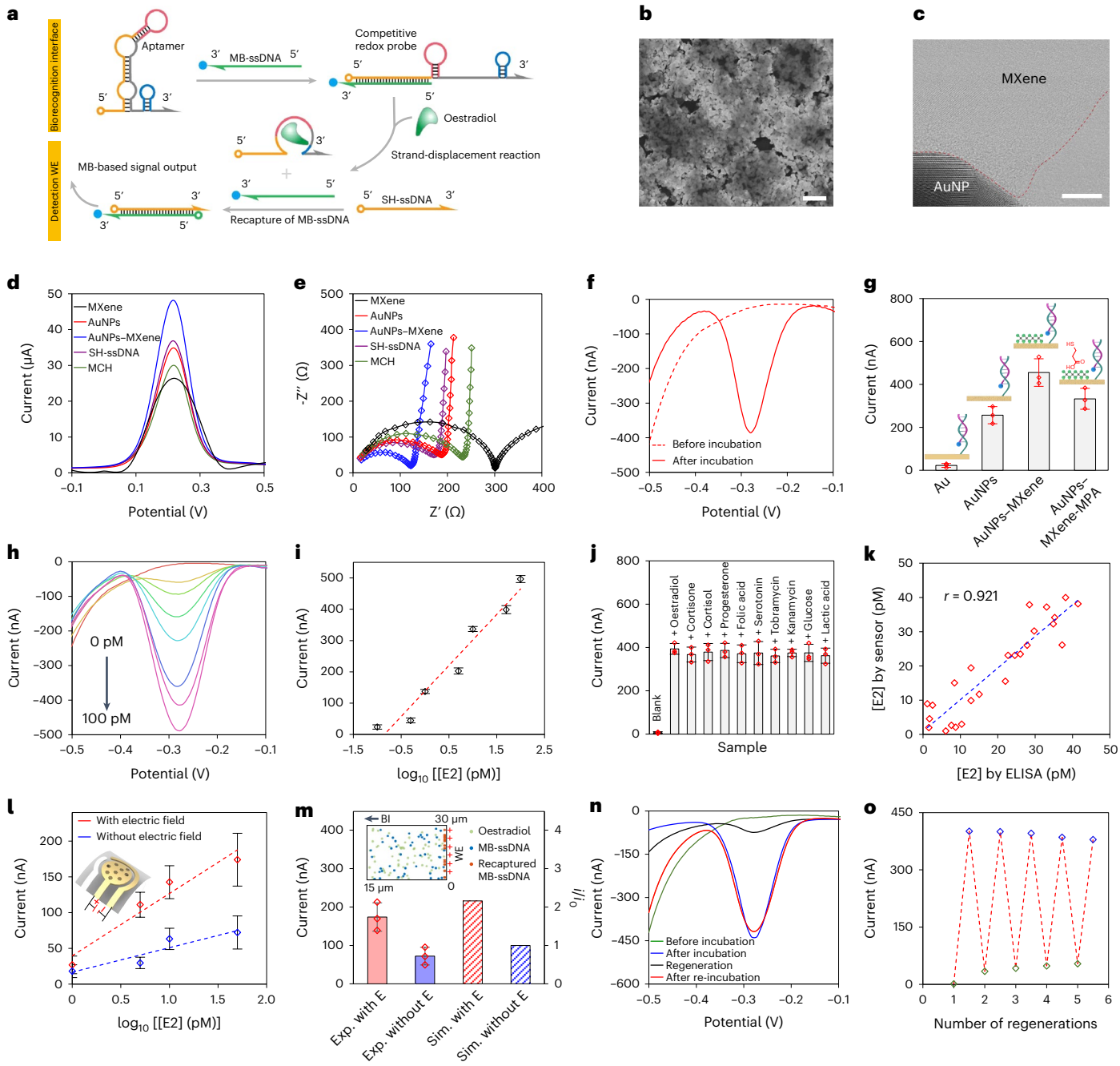


**Fig. 2 | Design and characterization of the reagentless amplification-free aptamer oestradiol sensor. a**, Schematic of the reagentless electrochemical aptamer sensor based on competitive redox probe displacement and recapture. **b**, SEM image of the inkjet-printed AuNPs–MXene electrode. The images are representative of three independent experiments. Scale bar, 200 nm. **c**, Transmission electron microscopy characterization of the AuNP–MXene. The images are representative of three independent experiments. Scale bar, 5 nm. **d**,**e**, DPV (**d**) and OCP–EIS (**e**) characterizations of the working electrode in 0.1× PBS (pH 7.4) containing 2.0 mM $K_4Fe(CN)_6/K_3Fe(CN)_6$ (1:1) after each surface-modification step: AuNPs, AuNPs–MXene, SH-ssDNA and MCH. **f**, SWV response of a modified AuNPs–MXene-based sensor before and after incubation with 50 pM of oestradiol. Z, Z' and Z'' represent impedance, resistance and reactance, respectively. **g**, Comparison of the detection performance of working electrode substrates including Au, AuNPs, AuNPs–MXene and AuNPs–MXene-MPA. Error bars represent the s.d. of the mean from three sensors. **h**,**i**, SWV response of the aptamer oestradiol sensors in artificial sweat (0.2× PBS, pH 7.4) with 0, 0.1, 0.5, 1, 5, 10, 50 and 100 pM of oestradiol (**h**) and the corresponding calibration plot based on the peak current height of the SWV voltammograms (**i**). Each SWV voltammogram was obtained from an independent oestradiol sensor (total eight sensors) in **h**. E2, oestradiol. Error bars represent the s.d. of the mean from three sensors. **j**, Selectivity of the aptamer sensor to potential interferences (50 pM) in human sweat. Error bars represent the s.d. of the mean from three sensors. **k**, Validation of the aptamer sensor towards oestradiol quantification in iontophoresis-induced human sweat samples with ELISA ($n = 25$). The dashed line represeonts the linear-fit trendline. $r$, linear correlation coefficient. **l**, Calibration plots of the aptamer sensors with 10 min of incubation measured with and without the assistance of an external electric field. Error bars represent the s.d. of the mean from three sensors. **m**, Experimental and simulation results of the sensor response with and without the assistance of an external electric field after 10 min of incubation. The inset shows simulated molecular diffusion and recapture of MB-ssDNA around the working electrode. Exp., experimental result; Sim., simulation result; E, electric field; BI, biorecognition interface. Error bars represent the s.d. of the mean from three sensors. **n**,**o**, The SWV voltammograms (**n**) and the corresponding peak current height (**o**) showing the regeneration and repetitive use of the aptamer oestradiol sensors with 50 pM of oestradiol. Error bars represent the s.d. of the mean from three sensors.

https://doi.org/10.1038/s41565-023-01513-0

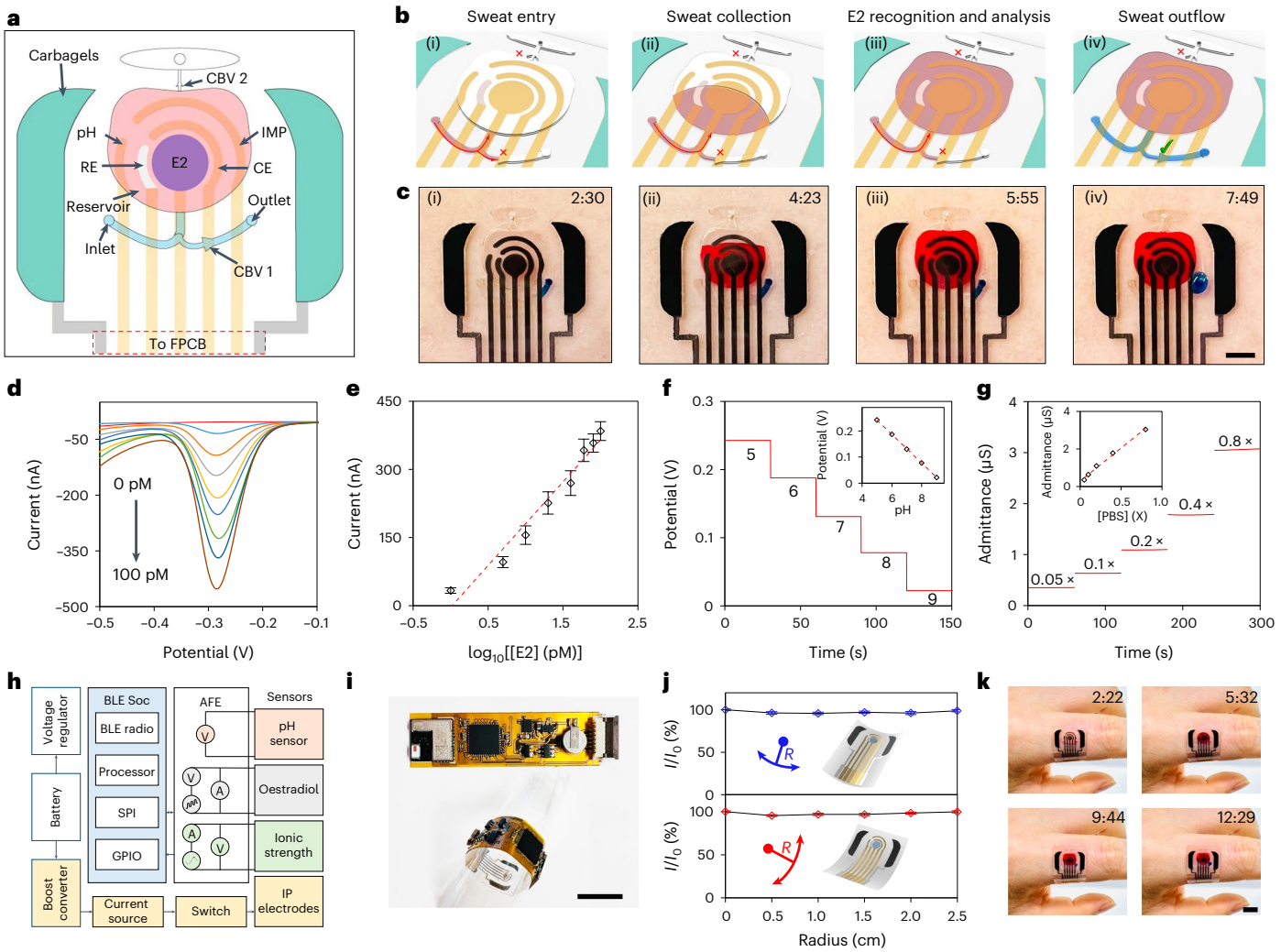


**Fig. 3 | Microfluidic wearable system integration for automatic in situ hormone analysis. a**, Schematic illustration of multiplexed microfluidic sensor patch for automatic reproductive hormone analysis. IMP, electrode for impedimetric ionic strength sensor. **b**,**c**, Schematic illustrations (**b**) and optical images (**c**) showing phases of CBV-modulated in situ sweat sampling process towards automatic oestradiol analysis: sweat entry via the inlet (i), sweat collection in the reservoir (ii), oestradiol recognition and analysis (iii) and sweat outflow via outlet (iv). Scale bar, 2.5 mm. **d**,**e**, The SWV voltammograms of the aptamer oestradiol sensors (**d**), and the corresponding calibration plot based on the peak current height (**e**) in a laboratory microfluidic flow test using artificial sweat (0.2× PBS, pH 7.4) containing 0, 1, 5, 10, 20, 40, 60, 80 and 100 pM of oestradiol. Error bars represent the s.d. of the mean from three sensors. **f**, Potentiometric response and corresponding calibration plot (inset) of the pH sensors in artificial sweat (0.2× PBS). **g**, Impedimetric response and the corresponding calibration plot (inset) of ionic strength sensors in artificial sweat (0.2× PBS, pH 7.4). **h**, Block diagram of wearable electronic system. IP, iontophoresis; GPIO, general-purpose input and output; SPI, serial peripheral interface; Soc, system-on-chip. **i**, Optical images of a fully integrated wearable system with high mechanical flexibility. Scale bar, 1 cm. **j**, performance of the aptamer sensor patch during the bending tests for both *x* and *y* axis. *I* and $I_0$ represent the peak current height of SWV voltammograms under and in the absence of mechanical deformation, respectively. R, radius of bending curvature. The error bars represent the s.d. of the mean from ten measurements in 50 pM oestradiol. **k**, Time-lapse images of the microfluidic sampling of the iontophoresis-induced sweat using a finger-worn wearable sensor for automatic hormone analysis. Scale bar, 5 mm.

and a high linear correlation coefficient of 0.921 between the ELISA and biosensor results was obtained.

Considering that the optimal incubation time for the competitive interaction and recapture is over 60 min, we explored the use of an external electric field (a positive potential bias between the working and counter electrodes before incubation) to reduce the incubation periods for rapid oestradiol analysis. Since ssDNA is negatively charged, applying a positive potential at the working electrode results in electrophoresis-based enhanced transport of the released MB-ssDNA redox probe across the sensing gap and substantially reduces the necessary incubation time (Supplementary Fig. 23a,b). As a result, electrochemical measurements reveal a substantially enhanced sensor signal after a 10 min incubation period with the application of a bias potential (1 min duration at +0.5 V before incubation) (Fig. 2l and Supplementary Fig. 24), in agreement with the numerical simulation results (Fig. 2m, Supplementary Fig. 23c,d and Supplementary Video 1). The applied bias potential leads to roughly 300 nA of current flowing through the electrodes (Supplementary Fig. 25). Thus, the power dissipation due to the low current flow is at the nW level. It should be noted that the hybridized MB-ssDNA dominates the signal of the final measurement while electrostatic adsorption or chelation of MB-ssDNA onto the positively charged detection working electrode only contributes to a small portion of the final measurement result (Supplementary Fig. 26). Considering that all free MB-ssDNA molecules result from the selective oestradiol-induced strand-displacement reaction, such electrostatic adsorption only contributes positively to sensitivity

https://doi.org/10.1038/s41565-023-01513-0

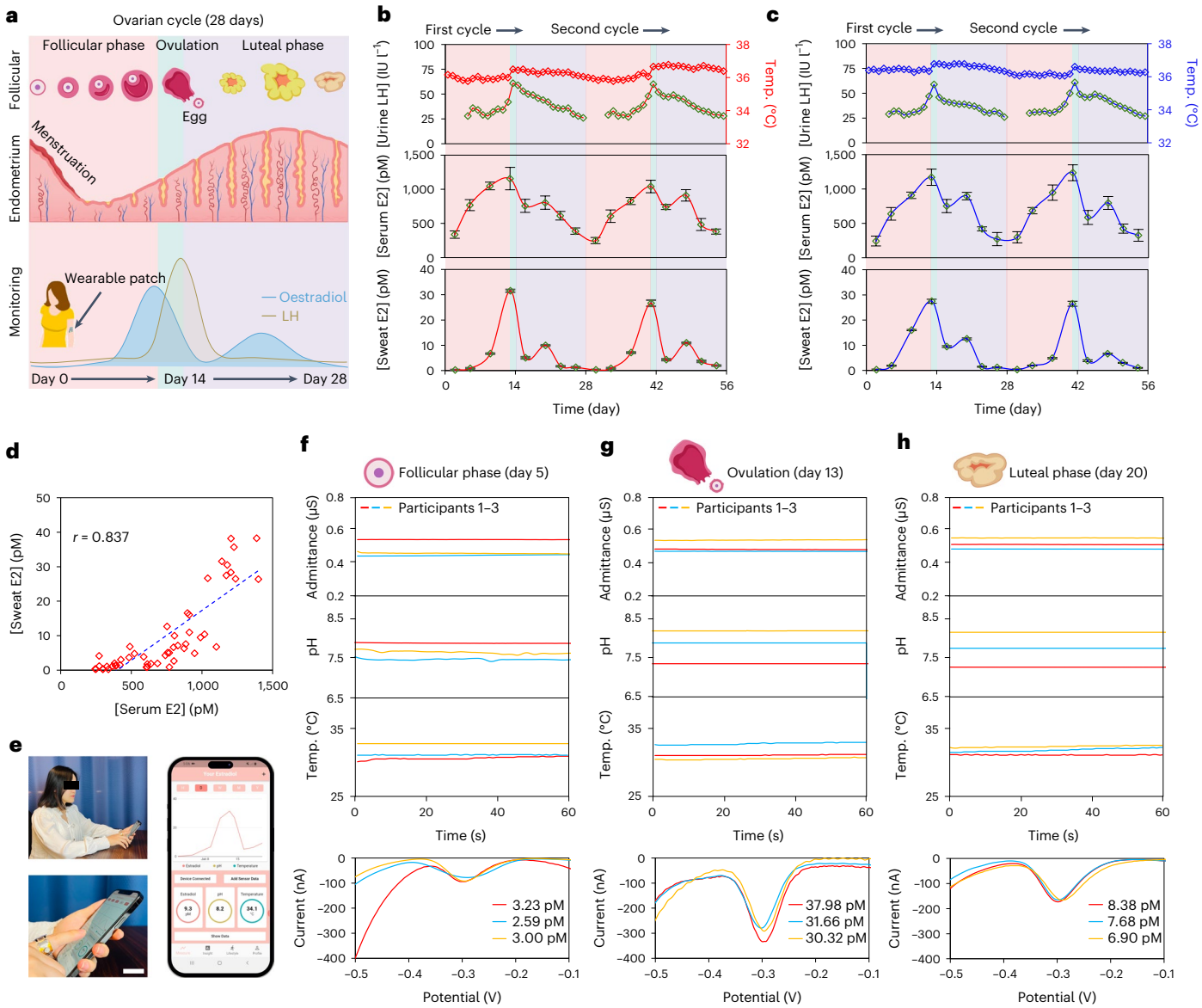


**Fig. 4 | Evaluation of the wearable sensor for non-invasive female hormone monitoring in human participants. a**, Hormonal fluctuations over the menstrual cycle. **b**,**c**, Continuous female hormone monitoring for two menstrual cycles in two female participants. Urine luteinizing hormone (LH) levels were tested by the commercial LH strips kit while oestradiol levels in serum and sweat were tested by the ELISA and the aptamer sensors, respectively. Error bars represent the s.d. of the mean from three measurements. Participant 1 was female, 32 years old (**b**) and participant 2 was female, 28 years old (**c**). **d**, Correlation of oestradiol levels between human sweat and serum ($n = 51$). Dashed line represents the linear-fit trendline. **e**, Optical images of a female human participant wearing the wireless wearable sensor during an on-body test. The collected data were wirelessly sent to a smartphone and displayed in the custom-developed mobile app. Scale bar, 1 cm. **f**–**h**, On-body multiplexed physicochemical sensing and oestradiol quantification with real-time sensor calibrations using the wearable aptamer sensor in the follicular (**f**), ovulation (**g**) and luteal (**h**) phases of menstrual cycles for three female human participants. Participant 1 was female, 31 years old; participant 2 was female, 28 years old and participant 3 was female, 32 years old. Temp., temperature.

without compromising sensor selectivity. The oestradiol sensor can be readily regenerated in deionized water (Fig. 2n) or in acidic conditions (Supplementary Fig. 27) after 1 min of incubation to perform repetitive oestradiol quantification (Fig. 2o). Successful oestradiol sensing and sensor regeneration showed only 6.2% signal drift after five cycles of repetitive measurement and/or regeneration (Fig. 2o and Supplementary Fig. 28).

## Automatic microfluidic oestradiol analysis

For automatic sweat oestradiol analysis in situ, we designed a disposable sensor patch consisting of a pair of carbachol gel-loaded inkjet-printed carbon electrodes for iontophoresis-based autonomous sweat induction[39], a microfluidic module coupled with one collection reservoir and two capillary bursting valves (CBVs) to precisely control the sweat sampling, and a multiplexed inkjet-printed sensor array in the microfluidic sensing reservoir for oestradiol quantification and calibration (Fig. 3a). The induced sweat will enter the microfluidic channel via the inlet, travel into and fill the sensing reservoir (with a sample volume of roughly 6.66 μl); when the sensing reservoir is filled, oestradiol analysis will initiate while newly secreted sweat is rerouted to the outlet due to capillary effects of the CBVs (Fig. 3b,c and Supplementary Fig. 29). Such microfluidic valving design allows highly stable biosensing in the quiescent sweat matrix free from the influence of sweat flow. Compared to the bulk solution analysis, no

apparent decrease in the sensitivity and selectivity of the oestradiol sensors was observed when operating in the microfluidics (Fig. 3d,e and Supplementary Figs. 30 and 31).

Considering that the large interindividual variability in sweat compositions (that is, pH and ionic strength) could have a major influence on the target recognition and electrochemical measurement, a polyaniline-based potentiometric pH sensor and an impedimetric ionic strength sensor were developed and integrated into the sensor patch. In vitro sensor evaluation revealed linear relationships between the measured potential and pH for the pH sensor, and between measured admittance and electrolyte levels for the ionic strength sensor (Fig. 3f,g). The accuracy of the pH sensor for sweat sample analysis was validated with a pH meter (Supplementary Fig. 32).

### Wireless wearable system integration and characterization

The fully integrated wearable oestradiol sensing system was developed based on the assembly of the disposable sensor patch and a reusable flexible printed circuit board (FPCB) (Fig. 3h and Supplementary Fig. 33). The FPCB contains a high compliance-voltage current source for iontophoresis to extract sweat on-demand and a programmable Bluetooth low lnergy (BLE) module that integrates a microcontroller for signal processing and wireless communication. To perform multiplexed sensing, this integrated system incorporates an electrochemical analogue front-end (AFE) that was able to perform multimodal electrochemical measurements (including voltammetry, impedimetry and potentiometry for oestradiol, pH, and ionic strength sensing, respectively). In addition, it could also provide skin temperature information continuously via a built-in temperature sensor in the AFE. During in situ sweat analysis, the obtained pH, ionic strength and skin temperature levels were used to calibrate the oestradiol sensor readings in real-time (Supplementary Fig. 34). A full measurement cycle consumes roughly 1 J in total (Supplementary Fig. 35); a rechargeable 3.8 V lithium coin cell battery with a capacity of 8 mAh could perform approximately 30 cycles. By exploring efficient wearable energy harvesting systems such as biofuel cells[40] and solar cells[41], it is possible to realize a fully self-powered wearable system.

The wearable patch was also designed to have high mechanical flexibility that enables conformal contact with the skin (Fig. 3i). It was able to maintain stable sensor responses under different bending radii, making it promising for practical at-home on-body monitoring during daily activities (Fig. 3j). When attached to the finger as a 'smart ring', the wearable system allowed efficient sweat extraction and sampling towards real-time oestradiol analysis (Fig. 3k, Supplementary Fig. 36 and Supplementary Video 2). Considering that the spot-checking of oestradiol every day is sufficient to monitor menstrual status, a disposable oestradiol sensor patch design coupled with a reusable wearable electronic system could fulfil the practical application needs of automatic, immediate and non-invasive oestradiol detection at any given time. When necessary, continuous wearable oestradiol sensing could be realized through integrating a multi-reservoir CBVs design[42] and oestradiol sensor arrays into a single sensor patch.

### In vivo evaluation of the wearable oestradiol sensor

During a menstrual cycle, oestradiol level in the blood rises and falls twice as illustrated in Fig. 4a: it gradually increases in the mid-follicular phase and reaches the highest point right before ovulation; then the oestradiol level drops quickly after ovulation, followed by a secondary rise during the mid-luteal phase and a secondary decrease at the end of the menstrual cycle[43]. Compared to invasive and lengthy blood assay, analysing sweat oestradiol using wearable technology offers a highly attractive approach for remote at-home female hormone monitoring (Fig. 4a). To validate the clinical values of the sweat oestradiol measured by the sensor, human studies were conducted over two consecutive menstrual cycles on two healthy female participants by simultaneously monitoring urine luteinizing hormone, body temperature and blood oestradiol (Fig. 4b,c). The results revealed that oestradiol levels in both sweat and serum reached the peak right before the ovulation while the urine luteinizing hormone and temperature levels peaked during the ovulation period, confirming oestradiol's potential for early ovulation prediction. The main and secondary rise of the oestradiol was also observed in both sweat and serum in all menstrual cycles. This indicates that sweat oestradiol follows cyclical fluctuation during the menstrual cycles. In addition, a strong correlation coefficient of 0.837 was identified between sweat and blood oestradiol levels from the pilot study (Fig. 4d), suggesting the high potential of sweat oestradiol as a non-invasive biomarker for fertility and ovulation monitoring.

On-body evaluation of the wearable technology for real-time in situ oestradiol analysis was performed on three female participants on day 5, day 13 and day 20 during a menstrual cycle with the sensor patch conformally attached onto the skin (Fig. 4e and Supplementary Video 3). During the study, sweat was induced via the built-in iontophoresis module, and sampled by the microfluidics. Multiplexed sensor data were collected wirelessly using a user interface (Fig. 4f–h). The calibrated oestradiol levels were converted in real time and displayed in a custom-developed mobile app based on the obtained multimodal data (Fig. 4e). As expected, the lowest oestradiol levels were observed on day 5 whereas the highest values appeared on day 13 in all participants; moderate oestradiol levels were observed on day 20 due to the secondary rise of the oestradiol during the menstrual cycle. Additional control studies were performed on three male participants; very low oestradiol levels were obtained on all participants with no apparent fluctuations (Supplementary Fig. 37).

## Conclusion

This work demonstrates an aptamer nanobiosensor with subpicomolar sensitivity for ultrasensitive and reagentless wearable analysis of the female hormone oestradiol in sweat. A AuNPs–MXene conductive scaffold enhanced signal transduction by enhancing the WE's electroactive surface area and charge transfer efficiency. For automatic on-body monitoring, a fully integrated wireless wearable system was designed that incorporates iontophoretic hydrogels for localized sweat stimulation, microfluidics for sweat collection and functionalized sensors for oestradiol sensing and calibration. We identified a direct correlation between sweat and serum oestradiol levels as well as clear cyclical fluctuation trends in sweat oestradiol levels during the menstrual cycle. This device thus enables convenient at-home reproductive hormone monitoring and can be reconfigured to monitor other trace-level biomarkers towards a wide variety of personalized medicine applications.

## Online content

Any methods, additional references, Nature Portfolio reporting summaries, source data, extended data, supplementary information, acknowledgements, peer review information; details of author contributions and competing interests; and statements of data and code availability are available at https://doi.org/10.1038/s41565-023-01513-0.

## References

1. Shansky, R. M. Are hormones a 'female problem' for animal research? *Science* **364**, 825–826 (2019).
2. Albert, P. R. Why is depression more prevalent in women? *J. Psychiatry Neurosci.* **40**, 219–221 (2015).
3. Nett, T. M., Turzillo, A. M., Baratta, M. & Rispoli, L. A. Pituitary effects of steroid hormones on secretion of follicle-stimulating hormone and luteinizing hormone. *Domest. Anim. Endocrinol.* **23**, 33–42 (2002).
4. Luine, V. N. Estradiol and cognitive function: past, present and future. *Horm. Behav.* **66**, 602–618 (2014).
5. van den Beld, A. W., de Jong, F. H., Grobbee, D. E., Pols, H. A. P. & Lamberts, S. W. J. Measures of bioavailable derum testosterone and estradiol and their relationships with muscle strength, bone density, and body composition in elderly men. *J. Clin. Endocr.* **85**, 3276–3282 (2000).

6. Knowlton, A. A. & Lee, A. R. Estrogen and the cardiovascular system. *Pharmacol. Ther.* **135**, 54–70 (2012).
7. Khosla, S., Oursler, M. J. & Monroe, D. G. Estrogen and the skeleton. *Trends Endocrinol. Metab.* **23**, 576–581 (2012).
8. Rosner, W., Hankinson, S. E., Sluss, P. M., Vesper, H. W. & Wierman, M. E. Challenges to the measurement of estradiol: an endocrine society position statement. *J. Clin. Endocrinol. Metab.* **98**, 1376–1387 (2013).
9. Karashima, S. & Osaka, I. Rapidity and precision of steroid hormone measurement. *J. Clin. Med.* **11**, 956 (2022).
10. Macsali, F. et al. Menstrual cycle and respiratory symptoms in a general Nordic–Baltic population. *Am. J. Respir. Crit. Care Med.* **187**, 366–373 (2013).
11. Rizk, B. & Smitz, J. Ovarian hyperstimulation syndrome after superovulation using GnRH agonists for IVF and related procedures. *Hum. Reprod.* **7**, 320–327 (1992).
12. Klaiber, E. L., Broverman, D. M., Vogel, W., Peterson, L. G. & Snyder, M. B. Relationships of serum estradiol levels, menopausal duration, and mood during hormonal replacement therapy. *Psychoneuroendocrinology* **22**, 549–558 (1997).
13. Geraci, A. et al. Sarcopenia and menopause: the role of estradiol. *Front. Endocrinol.* **12**, 682012 (2021).
14. Dey, S. et al. Cyclic regulation of sensory perception by a female hormone alters behavior. *Cell* **161**, 1334–1344 (2015).
15. Thienpont, L. M., Verhaeghe, P. G., Van Brussel, K. A. & De Leenheer, A. P. Estradiol-17 beta quantified in serum by isotope dilution-gas chromatography-mass spectrometry: reversed-phase C18 high-performance liquid chromatography compared with immuno-affinity chromatography for sample pretreatment. *Clin. Chem.* **34**, 2066–2069 (1988).
16. Stanczyk, F. Z., Jurow, J. & Hsing, A. W. Limitations of direct immunoassays for measuring circulating estradiol levels in postmenopausal women and men in epidemiologic studies. *Cancer Epidemiol. Biomark. Prev.* **19**, 903–906 (2010).
17. Lee, J. S. et al. Comparison of methods to measure low serum estradiol levels in postmenopausal women. *J. Clin. Endocrinol. Metab.* **91**, 3791–3797 (2006).
18. Ettinger, B. et al. Associations between low levels of serum estradiol, bone density, and fractures among elderly women: the study of osteoporotic fractures. *J. Clin. Endocrinol. Metab.* **83**, 2239–2243 (1998).
19. Ankarberg-Lindgren, C. & Norjavaara, E. A purification step prior to commercial sensitive immunoassay is necessary to achieve clinical usefulness when quantifying serum 17beta-estradiol in prepubertal children. *Eur. J. Endocrinol.* **158**, 117–124 (2008).
20. Seippel, L. & Bäckström, T. Luteal-phase estradiol relates to symptom severity in patients with premenstrual syndrome. *J. Clin. Endocr. Metab.* **83**, 1988–1992 (1998).
21. Yang, D. S., Ghaffari, R. & Rogers, J. A. Sweat as a diagnostic biofluid. *Science* **379**, 760–761 (2023).
22. Gao, W. et al. Fully integrated wearable sensor arrays for multiplexed in situ perspiration analysis. *Nature* **529**, 509–514 (2016).
23. Lee, H. et al. A graphene-based electrochemical device with thermoresponsive microneedles for diabetes monitoring and therapy. *Nat. Nanotechnol.* **11**, 566–572 (2016).
24. Yang, Y. et al. A laser-engraved wearable sensor for sensitive detection of uric acid and tyrosine in sweat. *Nat. Biotechnol.* **38**, 217–224 (2020).
25. Sempionatto, J. R. et al. An epidermal patch for the simultaneous monitoring of haemodynamic and metabolic biomarkers. *Nat. Biomed. Eng.* **5**, 737–748 (2021).
26. Ates, H. C. et al. End-to-end design of wearable sensors. *Nat. Rev. Mater.* **7**, 887–907 (2022).
27. Yang, Y. & Gao, W. Wearable and flexible electronics for continuous molecular monitoring. *Chem. Soc. Rev.* **48**, 1465–1491 (2019).
28. Sempionatto, J. R., Lasalde-Ramírez, J. A., Mahato, K., Wang, J. & Gao, W. Wearable chemical sensors for biomarker discovery in the omics era. *Nat. Rev. Chem.* **6**, 899–915 (2022).
29. Kim, J., Campbell, A. S., de Ávila, B. E.-F. & Wang, J. Wearable biosensors for healthcare monitoring. *Nat. Biotechnol.* **37**, 389–406 (2019).
30. Heikenfeld, J. et al. Accessing analytes in biofluids for peripheral biochemical monitoring. *Nat. Biotechnol.* **37**, 407–419 (2019).
31. Sinha, A. et al. MXene: an emerging material for sensing and biosensing. *Trends Anal. Chem.* **105**, 424–435 (2018).
32. Babar, Z. U. D., Della Ventura, B., Velotta, R. & Iannotti, V. Advances and emerging challenges in MXenes and their nanocomposites for biosensing applications. *RSC Adv.* **12**, 19590–19610 (2022).
33. UNAFold Web Server. *DNA Folding Form* (n.d.); http://www.unafold.org/mfold/applications/dna-folding-form.php
34. Zuker, M. Mfold web server for nucleic acid folding and hybridization prediction. *Nucleic Acids Res.* **31**, 3406–3415 (2003).
35. Rangel, A. E., Hariri, A. A., Eisenstein, M. & Soh, H. T. Engineering aptamer switches for multifunctional stimulus-responsive nanosystems. *Adv. Mater.* **32**, 2003704 (2020).
36. Pandey, R. et al. Integrating programmable DNAzymes with electrical readout for rapid and culture-free bacterial detection using a handheld platform. *Nat. Chem.* **13**, 895–901 (2021).
37. Li, J., Rossignol, F. & Macdonald, J. Inkjet printing for biosensor fabrication: combining chemistry and technology for advanced manufacturing. *Lab. Chip* **15**, 2538–2558 (2015).
38. VahidMohammadi, A., Rosen, J. & Gogotsi, Y. The world of two-dimensional carbides and nitrides (MXenes). *Science* **372**, eabf1581 (2021).
39. Wang, M. et al. A wearable electrochemical biosensor for the monitoring of metabolites and nutrients. *Nat. Biomed. Eng.* **6**, 1225–1235 (2022).
40. Yu, Y. et al. Biofuel-powered soft electronic skin with multiplexed and wireless sensing for human-machine interfaces. *Sci. Robot.* **5**, eaaz7946 (2020).
41. Min, J. et al. An autonomous wearable biosensor powered by a perovskite solar cell. *Nat. Electron.* **6**, 630–641 (2023).
42. Choi, J., Kang, D., Han, S., Kim, S. B. & Rogers, J. A. Thin, soft, skin-mounted microfluidic networks with capillary bursting valves for chrono-sampling of sweat. *Adv. Healthc. Mater.* **6**, 1601355 (2017).
43. Chenault, J. R., Thatcher, W. W., Kalra, P. S., Abrams, R. M. & Wilcox, C. J. Transitory changes in plasma progestins, estradiol, and luteinizing hormone approaching ovulation in the bovine. *J. Dairy Sc.* **58**, 709–717 (1975).

# Methods

## Materials and reagents

β-Oestradiol, cortisone, progesterone, folic acid, serotonin, cortisol, tobramycin, kanamycin, glucose, lactic acid, MCH, 3-MPA, potassium ferrocyanide(II), tris(hydroxymethyl)aminomethane hydrochloride (Tris-HCl), tris-(2-carboxyethyl)-phosphine hydrochloride (TCEP) and EDTA were purchased from Sigma-Aldrich. Magnesium chloride, potassium chloride, isopropyl alcohol, ethylene glycol, sulfuric acid and sodium chloride, were purchased from Fisher Scientific. The ELISA kit for oestradiol was purchased from Invitrogen. Iron(III) chloride, potassium ferricyanide(III), silver nitrate and 0.1 M phosphate-buffered saline (PBS) (pH 7.4) were purchased from Alfa Aesar. Medical adhesives were purchased from Adhesives Research and 3M. Polyethylene terephthalate (PET) films were purchased from McMaster-Carr. The oestradiol aptamer and other DNA oligonucleotides with an initial concentration of 100 μM were ordered from Integrated DNA Technologies (detailed sequences shown in Supplementary Fig. 6a). Carbon ink (5 wt%) and silver ink (25 wt%) were purchased from NovaCentrix. Gold ink (10 wt%) was purchased from C-INK Co. Ltd. All chemicals are used as received. Screen-printed Au electrodes were purchased from Shenzhen Haoyang Technology Co., Ltd (HY-PA100). Plain Au electrodes (as the control) were fabricated on a PET substrate by photolithography and electron-beam evaporation (30 nm Cr/100 nm Au).

## Preparation of the MXene nanosheets ink

MXene nanosheets were synthesized using the minimally intensive layer delamination method[44]. First, 2 g of lithium fluoride was dissolved in 40 ml of 9 M HCl, then 1 g of $Ti_3AlC_2$ MAX phase powder was gradually added into the etchant under continuous stirring at room temperature. The mixture proceeded to react for 48 h at 40 °C under continuous stirring. Once the reaction was completed, the acidic mixture was washed multiple times with deionized water by centrifugation at 2,044 relative centrifugal force (RCF) for 5 min for each cycle until the pH turned neutral. The dark-green supernatant was discarded, and 20 ml of deionized water was added to the sediment. This was followed by vigorous shaking using a vortex machine for 1 h. The dispersion was then centrifuged at 327 RCF for 5 min and the supernatant was collected. The suspension containing exfoliated MXene nanosheets was centrifuged again at 2,044 RCF to remove the residual impurities. Next, 10 ml of deionized water was added to the sediment and an MXene suspension with a concentration of roughly 15 mg $ml^{-1}$ was obtained. To prepare the MXene ink, an aliquot of the MXene suspension was diluted to a concentration of 2 mg $ml^{-1}$. The suspension was then probe sonicated for 1 h under the protection of $N_2$ to reduce the size of the nanosheets. The suspension was then filtered using a 0.45 μm filter and ethylene glycol was added in a volume ratio of 1:1.

## Fabrication and characterization of disposable sensor patch

The fabrication procedures of the inkjet-printed sensor patch are illustrated in Supplementary Fig. 3. First, the PET substrate was washed with isopropyl alcohol and dried using compressed air flow. The PET substrate was treated with 10 min of $O_2$ plasma using Plasma Etch PE-25 (20–30 $cm^3$ $min^{-1}$ $O_2$, 100 W, 150 to 200 mTorr) to enhance the surface hydrophilicity. The multimodal sensor patch was fabricated via serial printing of gold (reference, working and counter electrodes, pH sensor and ionic strength sensor), silver (interconnects and reference electrode), carbon (iontophoresis electrodes) and MXene (WE) using an inkjet printer (DMP-2850, Fujifilm). The thickness of MXene layer is crucial to the sensor performance (Supplementary Fig. 15) and four-layer MXene printing coupled with two-layer Au printing was determined to be optimal. The plate temperature was set to 40 °C to ensure the rapid ink solvent vaporization during printing.

The morphology and material properties were characterized by transmission electron microscopy (Talos S-FEG FEI) and SEM (Nova Nano SEM 450). The Raman spectrum of the electrodes was recorded using a 532.8 nm laser with an inVia Reflex (Renishaw). X-ray diffraction patterns were recorded with an X-ray diffractometer (D/max-Ultima IV).

## Construction and modification of sensing platform

The biorecognition interface and working electrode were assembled face-to-face on the sensing patch. We first diluted both of thiol-modified aptamer-ssDNA and SH-ssDNA to 5 μM with 20 mM Tris-HCl buffer (containing 50 mM NaCl and 25 mM $MgCl_2$, pH 8.0), and then reduced them for 3 h in a solution of 500 μM TCEP at room temperature in the dark. To form the aptamer's functional secondary structure, the oestradiol aptamer-ssDNA was then heated at 95 °C for 5 min and then cooled down slowly to room temperature. As shown in Supplementary Fig. 8, SH-ssDNA (5 μM, 2 μl) and aptamer-ssDNA (5 μM, 2 μl) were immobilized onto the inkjet-printed AuNPs–MXene (WE) and AuNPs (biorecognition interface), respectively, via the Au–SH binding overnight, respectively. MCH (100 mM, 2 μl) was used to block the unbound active sites of AuNPs for 30 min, subsequently, followed by rinsing with deionized water to wash away the non-electrostatically adsorbed ssDNA and aptamer-ssDNA. Then, the redox probe MB-ssDNA (1 μM, 2 μl) was attached to the biorecognition interface for 30 min to form a partially hybridized duplex with an aptamer-ssDNA, which acts as a competitive redox probe.

The pH sensing electrode was prepared by electrodeposition of polyaniline pH sensing membrane on the inkjet-printed Au electrode by means of cyclic voltammetry between −0.2 and 1.2 V at a scan rate of 0.1 V $s^{-1}$ for 25 cycles.

## Electrochemical characterizations of the biosensors

SWV, cyclic voltammetry, differential pulse voltammetry (DPV) and OCP–EIS were carried out on a CHI820 electrochemical station. All the electrochemical measurements were performed at room temperature in artificial sweat (0.2× PBS, pH 7.4 unless otherwise noted) and SWV was performed over a voltage range of 0 to −0.6 V at a frequency of 90 Hz (unless otherwise noted). To characterize the sensor performance, oestradiol was introduced in between the biorecognition interface and working electrode for 90 min of incubation (unless otherwise noted). The limit of detection was calculated on the basis of the mean of the blank, the standard deviation of the blank, the sensitivity and a defined confidence factor of 3.2 (for a confidence of 95%).

To characterize the electrode performances of screen-printed Au, Au, AuNPs and AuNPs–MXene, and to confirm the surface modification after each step, DPV and OCP–EIS readings were executed in 0.1× PBS (pH 7.4) containing 2.0 mM $K_4Fe(CN)_6/K_3Fe(CN)_6$ (1:1) under the following conditions: potential range, −0.2–0.6 V; pulse width, 0.2 s; incremental potential, 4 mV; amplitude, 50 mV; frequency range, 0.1–106 Hz; amplitude, 5 mV. $[Fe(CN)_6]^{3-}$–$[Fe(CN)_6]^{4-}$ was chosen as the redox couple for electrochemically monitoring the stepwise modification of electrode surfaces owing to its low redox potential, low surface contamination and negative charge for optimal electrode performance characterization[45–47]. In addition, the electrode surfaces of Au, AuNPs and AuNPs–MXene were compared through cyclic voltammetry characterization in the range of 0.5 to 0.7 V at different scan rates (5, 10, 50, 100, 150 and 200 mV $s^{-1}$) in artificial sweat (0.2× PBS, pH 7.4).

The electrodes used in these studies were prepared on the same day and stored at 4 °C (unless otherwise noted). To shorten the incubation time by enhancing the molecular transport, a bias potential (1 min duration at +0.5 V) could be applied before the incubation between working electrode and counter electrode.

## Numerical simulation of electric field enhanced bioanalysis

Numerical simulation of the chemical reaction and mass transport of oestradiol and MB-ssDNA were conducted by the Monte Carlo method using MATLAB R2020b. Initially, oestradiol molecules were randomly distributed in the 0.335 × 4 $mm^2$ 2D rectangular area and doing a random walk. Once oestradiol reached the biorecognition interface, it

could be captured by the aptamer-ssDNA, resulting in the release of MB-ssDNA; the probability here, $P_1$, was set to be $6 \times 10^{-3}$ (value was chosen according to the experimental data). The released MB-ssDNA will also do a random walk in the system. The mean-squared displacement (m.s.d.) of species in the system is described by:

$$\text{m.s.d.} = (\Delta x)^2 = 4D \times \Delta t$$

where $\Delta x$ is the displacement within one time step $\Delta t$, and $D$ is the diffusion coefficient. Here, the time step was set at 1 s, and the diffusion coefficients of oestradiol and MB-ssDNA were $6.2 \times 10^{-10}$ and $5.0 \times 10^{-11}$ m$^2$ s$^{-1}$, respectively[48,49]. Once an MB-ssDNA reached the working electrode, there was a probability $P_2$ for the MB-ssDNA molecule to be captured by a complementary DNA on the working electrode within one time step. Since MB-ssDNA is a large molecule, the effective binding sites are limited. Each bound MB-ssDNA will occupy one effective reaction site, affecting the surrounding complementary DNAs to capture methylene blue due to steric hindrance. So, the capture probability of the working electrode is:

$$P_2 = k_{\text{capture}} \times \left(1 - \frac{n_{\text{bounded}}}{n_{\text{initial}}}\right)^2 \times \Delta t$$

where $k_{\text{capture}}$ is a constant and was set to be $2 \times 10^{-3}$ s$^{-1}$, $n_{\text{initial}}$ is the initial number of effective bound sites and was set to be $3.2 \times 10^6$, and $n_{\text{bounded}}$ is the number of effective bound sites already bound to MB-ssDNA ($k_{\text{capture}}$ and $n_{\text{initial}}$ values were chosen to match the experimental data without electric field). Since the binding process is reversible, for each bound MB-ssDNA, there is a probability $P_3$ that it will be released from the working electrode and here we set $P_3$ to be:

$$P_3 = k_{\text{release}} \times \Delta t$$

where $k_{\text{release}}$ is a constant and was set to be $1.3 \times 10^{-3}$ s$^{-1}$.

The electrophoresis velocity of MB-ssDNA is described by:

$$v = \mu \times E$$

where $\mu$ is the electrophoretic mobility of MB-ssDNA, which was set to be $3.4 \times 10^{-8}$ m$^2$ (V s)$^{-1}$ (ref. 50) and $E$ is the electric field strength in the system. Since discharging is going to occur in the system, the electric field strength is described by:

$$E = E_0 \times e^{-\frac{t}{t_c}}$$

where $E_0$ is electric field strength at $t = 0$ and was set to be $4.5 \times 10^{-2}$ V mm$^{-1}$, and $t_c$ is a constant and was set to be 20 min.

### Fabrication and characterization of microfluidics

A 50 W $CO_2$ laser cutter (Universal Laser System) was used to fabricate the microfluidic module. For all microfluidic layers, the iontophoresis gel outlines were patterned to enable the contact between the hydrogel and the skin. The bottom accumulation layer (the double-sided adhesive layer in contact with the skin) was patterned with a sweat accumulation chamber (130 µm 3M 468MP, laser parameters: power 60%, speed 90%, PPI 1,000) and microchannels including the CBVs. The chamber has an ellipse shape (6.4 mm in the minor axis and 7.5 mm in the major axis) to fully enclose the sweat collection reservoir. The dimension of the CBVs is demonstrated in Supplementary Fig. 29. The second layer as the biorecognition interface with the inkjet-printed AuNPs was patterned with an inlet (100 µm-thick PET, laser parameters: power 30%, speed 90%, PPI1,000). For the third layer (collection layer) in contact with the biorecognition interface layer, an assembly of PET film with the thickness of 75 µm sandwiched between double-sided medical adhesives (130 µm 3 M 468MP) was cut through to make the inlet and outlet, channels with CBVs and sweat collection reservoir (laser parameters: power 60%, speed 75%, PPI1,000). The thickness of the collection layer was roughly 335 µm, the reservoir area was roughly 19.87 mm$^2$ and the reservoir volume totalled roughly 6.66 µl, which was calculated as the area multiplied by the thickness of the reservoir layer.

### Fabrication of iontophoresis hydrogels

The iontophoresis hydrogels on the anode and cathode were made of agarose (3% w/w). The agarose was fully dissolved in deionized water and then heated to 250 °C. Then, 1% carbachol as the muscarinic agents for the anode hydrogel and 1% KCl for the cathode hydrogel were added when the solution was cooled down to 165 °C. Subsequently, the mixture was slowly cast into the microfluidic patch and solidified for 10 min at room temperature. The prepared hydrogels were stored at 4 °C for long-term use.

### Electronic system design and integration

A FPCB with two layers was created using Eagle CAD and Fusion 360. The FPCB has a rectangular shape (13 × 46 mm$^2$) that can be wrapped around a finger-like a ring. The electronic system of the FPCB includes a voltage regulator (ADP162, Analog Devices) for power management; a boost converter (TPS61096, Texas Instruments), bipolar junction transistor array (BCV62C, Nexperia) and analogue switch (DG468, Vishay Intertechnology) for iontophoretic sweat induction; an AFE (AD5941, Analog Devices) and an operational amplifier (LPV811, Texas Instruments) for the sensor interface and a BLE module (CYBLE-222014-01, Cypress Semiconductor) programmed through PSoC Creator v.4.3 for controlling the system and enabling wireless communication. Through its general-purpose input and output pins, the BLE module initiates current flow through the iontophoresis electrodes for sweat stimulation. The iontophoresis setup is designed to apply 55 µA across the skin with a compliance voltage of 18 V such that it can function across a wide range of skin impedances. Furthermore, the current goes through a switch and is interfaced with a transimpedance amplifier within the electrochemical AFE to monitor the current that is applied during iontophoresis, and to shut the current off if the current source malfunctions and applies a current above 55 µA. After stimulation, the BLE module controls the AFE to perform electrochemical techniques such as potentiometry, impedimetry and SWV to acquire sensor data. After a certain amount of sensor data have been piled up in the AFE's internal memory, the AFE interrupts to BLE module to fetch and transmit the sensor data to a customized mobile application or a BLE dongle (CY5677, Cypress Semiconductor) for data processing and display.

The power consumption profiles of the wearable system are demonstrated in Supplementary Fig. 34. During operation, the electronic system is connected to a user interface over BLE with a connection interval of 0.25 s. Iontophoresis consumes around 2.7 mW for 5 min. Before incubation, an electric field is applied for 1 min, where 0.5 V is applied and the resulting current is measured with a sampling interval of 2 s. During the electric field application, the system that operates at 3 V consumes an average power of roughly 695 µW for 1 min. During the incubation, the system goes to idle mode where a BLE connection interval of 4 s is maintained to consume a power of roughly 100 µW. Then, SWV is performed, where an average power of roughly 11.3 mW is applied for 2.3 s. Finally, simultaneous ionic strength, pH and temperature measurements, with a sampling interval of 2 s, are applied for 1 min consuming an average power of roughly 1.8 mW.

### Human participant recruitment

The evaluation of the wearable technology for non-invasive female hormone monitoring in sweat and serum samples for human participants followed all the ethical regulations according to the protocol (ID 19-0892), which was approved by the Institutional Review Board at California Institute of Technology (Caltech). The participating participants (age range 18–65 years; premenopausal) were recruited from Caltech

campus and the neighbouring communities through advertisement by posted notices, word of mouth and email distribution. All participants gave written informed consent before participation in the study.

For sweat collection (used for in vitro sensor validation), an iontophoresis session was performed on the participants using a Macroduct Sweat Collection System (Model 3700) to induce sweat. A Macroduct collector was then used to collect sweat sample over a period of 20 min. Fresh blood samples were collected at the same period of sweat collection using a finger-prick approach. After the clotting procedure, serum was separated by centrifuging (15 min at 1,044 RCF) and instantly stored at −80 °C.

### Human samples with the ELISAs

ELISA tests for oestradiol analysis in serum and sweat samples were performed in an accuSkan FC Filter-Based Microplate Photometer at a detection wavelength of 450 nm according to the manufacturer's instructions. In brief, 50 µl of standard, control or samples were added to microtiter plate wells, and then 50 µl of oestradiol–horseradish peroxidase conjugate and 50 µl of anti-oestradiol were added into all wells in sequence. The plate with this mixture was covered with aluminium foil or metalized mylar and incubated for 2 h at room temperature on a horizontal shaker set at 1.372 ± 0.0168 RCF. After washing four times with wash buffer, 200 µl of chromogen solution (3,3′,5,5′-tetramethylbenzidine) was added into each well, in which the liquid in the wells turned blue on reaction. This was then incubated for 30 min at room temperature in the dark, and the absorbance values were measured immediately after the addition of stop solution (50 µl, 1 M $H_2SO_4$) in each well.

### Evaluate the wearable oestradiol sensor in human participants

To evaluate the wearable aptamer sensor for sweat oestradiol analysis and investigate the clinical values of sweat oestradiol, female participants were recruited with periodic female hormone monitoring for two consecutive menstrual cycles. During each day of study, we collected self-reported urine luteinizing hormone level analysed by the participants with a commercial strip kit, body temperature monitored with a medical thermometer, serum oestradiol (serum samples were collected via invasive blood draw and analysed with ELISA kits) and sweat oestradiol (sweat samples were collected via iontophoresis and analysed with the aptamer sensors).

For on-body system validation, the participants were arranged with multiplexed physicochemical sensing and oestradiol quantification with real-time sensor calibrations using the wearable aptamer sensor in the follicular, ovulation, luteal phases of menstrual cycles. The participants' arms and fingers were cleaned with alcohol swabs, and after 5 min of iontophoresis applied to the participants, the aptamer sensor patch performed sweat sampling, incubation and biosensing for 60 min. During the on-body trial, the collected SWV data and the physical data, including temperature, pH and impedance, were wirelessly transmitted to a user device via BLE in real time from which the molecular data were extracted, calibrated and converted to concentration levels. Microsoft Excel v.2016 was used to analyse all data, plot the data and calculate the statistical parameters.

### Reporting summary

Further information on research design is available in the Nature Portfolio Reporting Summary linked to this article.

## Data availability

The main data supporting the results in this study are available within the paper and its Supplementary Information. Source data for Figs. 2–4 are provided with this paper.

## References


44. Alhabeb, M. et al. Guidelines for synthesis and processing of two-dimensional titanium carbide ($Ti_3C_2T_x$ MXene). *Chem. Mater.* **29**, 7633–7644 (2017).
45. Torrente-Rodríguez, R. M. et al. Investigation of cortisol dynamics in human sweat using a graphene-based wireless mHealth system. *Matter* **2**, 921–937 (2020).
46. Capatina, D. et al. Label-free electrochemical aptasensor for the detection of the 3-O-C12-HSL quorum-sensing molecule in *Pseudomonas aeruginosa*. *Biosensors* **12**, 440 (2022).
47. Torrente-Rodríguez, R. M. et al. SARS-CoV-2 RapidPlex: a graphene-based multiplexed telemedicine platform for rapid and low-cost COVID-19 diagnosis and monitoring. *Matter* **3**, 1981–1998 (2020).
48. Frum, Y., Bonner, M. C., Eccleston, G. M. & Meidan, V. M. The influence of drug partition coefficient on follicular penetration: In vitro human skin studies. *Eur. J. Pharm. Sci.* **30**, 280–287 (2007).
49. Sparrenberg, L. T., Greiner, B. & Mathis, H. P. Bleaching correction for DNA measurements in highly diluted solutions using confocal microscopy. *PLoS ONE* **15**, e0231918 (2020).
50. Salieb-Beugelaar, G. B., Dorfman, K. D., van den Berg, A. & Eijkel, J. C. T. Electrophoretic separation of DNA in gels and nanostructures. *Lab. Chip* **9**, 2508 (2009).


## Acknowledgements

This project was supported by the National Institutes of Health grant nos. R01HL155815 and R21DK13266, National Science Foundation grant no. 2145802, Office of Naval Research grant nos. N00014-21-1-2483 and N00014-21-1-2845, American Cancer Society Research Scholar grant no. RSG-21-181-01-CTPS and a Sloan Research Fellowship. We gratefully acknowledge critical support and infrastructure provided for this work by the Kavli Nanoscience Institute at Caltech.

## Author contributions

W.G. and C.Y. initiated the concept and designed the overall studies. W.G. supervised the work. C.Y. and M.W. led the experiments and collected the overall data. J.M., R.Y.T., H.L., J.R.S. and C.X. contributed to sensor characterization and validation. J.L. contributed to the numerical simulation. All authors contributed the data analysis and provided feedback on the manuscript.

## Competing interests

The authors declare no competing interests.

## Additional information

**Supplementary information** The online version contains supplementary material available at https://doi.org/10.1038/s41565-023-01513-0.

**Correspondence and requests for materials** should be addressed to Wei Gao.

**Peer review information** *Nature Nanotechnology* thanks Fabiana Arduini, Eden Morales-Narvaez and the other, anonymous, reviewer(s) for their contribution to the peer review of this work.

nature research

Corresponding author(s): Wei Gao

Last updated by author(s): Aug 14, 2023

# Reporting Summary

Nature Research wishes to improve the reproducibility of the work that we publish. This form provides structure for consistency and transparency in reporting. For further information on Nature Research policies, see our Editorial Policies and the Editorial Policy Checklist.

## Statistics

For all statistical analyses, confirm that the following items are present in the figure legend, table legend, main text, or Methods section.

| n/a | Confirmed | |
|---|---|---|
| ☐ | ☒ | The exact sample size (*n*) for each experimental group/condition, given as a discrete number and unit of measurement |
| ☐ | ☒ | A statement on whether measurements were taken from distinct samples or whether the same sample was measured repeatedly |
| ☒ | ☐ | The statistical test(s) used AND whether they are one- or two-sided<br>*Only common tests should be described solely by name; describe more complex techniques in the Methods section.* |
| ☒ | ☐ | A description of all covariates tested |
| ☒ | ☐ | A description of any assumptions or corrections, such as tests of normality and adjustment for multiple comparisons |
| ☐ | ☒ | A full description of the statistical parameters including central tendency (e.g. means) or other basic estimates (e.g. regression coefficient) AND variation (e.g. standard deviation) or associated estimates of uncertainty (e.g. confidence intervals) |
| ☒ | ☐ | For null hypothesis testing, the test statistic (e.g. *F*, *t*, *r*) with confidence intervals, effect sizes, degrees of freedom and *P* value noted<br>*Give P values as exact values whenever suitable.* |
| ☒ | ☐ | For Bayesian analysis, information on the choice of priors and Markov chain Monte Carlo settings |
| ☒ | ☐ | For hierarchical and complex designs, identification of the appropriate level for tests and full reporting of outcomes |
| ☐ | ☒ | Estimates of effect sizes (e.g. Cohen's *d*, Pearson's *r*), indicating how they were calculated |

*Our web collection on statistics for biologists contains articles on many of the points above.*

## Software and code

Policy information about availability of computer code

| | |
|---|---|
| Data collection | Mbed was used to program microcontroller. CH Instrument was used for off-body sensor data collection. MATLAB R2020b with Monte-Carlo method was used for simulations. |
| Data analysis | Microsoft Excel 2016 was used to analyze all data, plot the data and calculate the statistical parameters. |

For manuscripts utilizing custom algorithms or software that are central to the research but not yet described in published literature, software must be made available to editors and reviewers. We strongly encourage code deposition in a community repository (e.g. GitHub). See the Nature Research guidelines for submitting code & software for further information.

## Data

Policy information about availability of data

All manuscripts must include a data availability statement. This statement should provide the following information, where applicable:

- Accession codes, unique identifiers, or web links for publicly available datasets
- A list of figures that have associated raw data
- A description of any restrictions on data availability

The main data supporting the results in this study are available within the paper and its Supplementary Information. Source data for Figs. 2, 3, and 4 are provided with this paper. All raw and analysed datasets generated during the study are available from the corresponding author on request.

# Field-specific reporting

Please select the one below that is the best fit for your research. If you are not sure, read the appropriate sections before making your selection.

☒ Life sciences ☐ Behavioural & social sciences ☐ Ecological, evolutionary & environmental sciences

For a reference copy of the document with all sections, see nature.com/documents/nr-reporting-summary-flat.pdf

# Life sciences study design

All studies must disclose on these points even when the disclosure is negative.

| | |
|---|---|
| Sample size | For on body evaluation of the wearable sensor, 6 subjects (3 female premenopausal subjects and 3 male subjects at the age range from 18 to 65 years old ) were involved. Sample sizes were chosen on the basis of literature standards for proof-of-concept experiments. |
| Data exclusions | No data exclusion. |
| Replication | Results were replicated in independent experiments as described in the manuscript.<br>Every experiment included replicates as described in the figure legends and experimental methods. |
| Randomization | The device was fabricated with same process and was tested in all participants under same conditions. Randomization was therefore not relevant to the study. |
| Blinding | Not relevant, because a blinding process wouldn't influence the sampling result. |

# Reporting for specific materials, systems and methods

We require information from authors about some types of materials, experimental systems and methods used in many studies. Here, indicate whether each material, system or method listed is relevant to your study. If you are not sure if a list item applies to your research, read the appropriate section before selecting a response.

## Materials & experimental systems

| n/a | Involved in the study |
|---|---|
| ☒ | ☐ Antibodies |
| ☒ | ☐ Eukaryotic cell lines |
| ☒ | ☐ Palaeontology and archaeology |
| ☒ | ☐ Animals and other organisms |
| ☐ | ☒ Human research participants |
| ☒ | ☐ Clinical data |
| ☒ | ☐ Dual use research of concern |

## Methods

| n/a | Involved in the study |
|---|---|
| ☒ | ☐ ChIP-seq |
| ☒ | ☐ Flow cytometry |
| ☒ | ☐ MRI-based neuroimaging |

## Human research participants

Policy information about studies involving human research participants

| | |
|---|---|
| Population characteristics | Healthy subjects were recruited. Inclusion criteria were: female premenopausal subjects and male subjects aged 18-65 years; BMI between 18–40 kg m-2. Exclusion criteria included: significant chronic disease; severe and/or uncontrolled medical conditions that could interfere with the study; malignancy within the previous 2 years; HIV infection; active tuberculosis; documented cardiovascular disease or resting ECG abnormality; use of systemic corticosteroids; those requiring supplemental oxygen; adult patients with a diagnosis of heart failure, pregnancy, severe skin allergy, current need for inpatient hospitalization, current use of beta-blocker medication therapy due to theoretical interaction with pilocarpine, active inotropic medication infusion, hypotension or hypertension, severe bradycardia or tachycardia, or significant cardiac conduction disorder; patients admitted to the hospital ≥18 years of age that had an active infection (e.g., pneumonia, UTI, cellulitis, etc.). |
| Recruitment | The participating subjects were recruited from Caltech campus, and the neighboring communities through advertisement by posted notices, word of mouth, and email distribution. There were no self-selection biases or other biases. All participants gave written informed consent before participation in the study. |
| Ethics oversight | California Institute of Technology |

Note that full information on the approval of the study protocol must also be provided in the manuscript.